Temperature-dependent phonon anharmonicity and thermal transport in $CuInTe_2$

Hao Yu,[1,2] Liu-Cheng Chen,[1,2] Hong-Jie Pang,[2] Peng-Fei Qiu,[3] Qing Peng,[1,4,*] and Xiao-Jia Chen[1,2,†]

[1]*School of Science, Harbin Institute of Technology, Shenzhen 518055, China*

[2]*Center for High Pressure Science and Technology Advanced Research, Shanghai 201203, China*

[3]*State Key Laboratory of High Performance Ceramics and Superfine Microstructure, Shanghai Institute of Ceramics, Chinese Academy of Sciences, Shanghai 200050, China*

[4]*State Key Laboratory of Nonlinear Mechanics, Institute of Mechanics, Chinese Academy of Sciences, Beijing 100190, China*

(Received 22 November 2021; revised 9 May 2022; accepted 22 June 2022; published 28 June 2022)

The Cu-based chalcopyrite compounds are good thermoelectrics for waste heat harvesting, partially due to the dramatic reduction of the thermal conductivity above Debye temperature, whereas the mechanism of this drop is still elusive. By Raman measurements from 7 to 780 K, we have investigated the anharmonicity of the phonon modes B_2^1, A_1, and B_2^3 in $CuInTe_2$. The fourth-order anharmonicity of B_2^1 and B_2^3 modes is greatly enhanced with increasing temperature and becomes dominant above 400 K. The phonon dynamics is calculated from 10 to 800 K. The fourth-order anharmonicity is predominant over the third-order ones for the phonon modes at low (<70 cm^{-1}) and high (>130 cm^{-1}) frequency domains, confirmed by the enhanced weighted phase space and scattering rate of the four-phonon processes above 300 K. The phonon avoided-crossing is found to take place around 40 cm^{-1} between the lowest-optical mode and acoustic modes. Counting on the fourth-order phonon anharmonicity, the calculated lattice thermal conductivity agrees well with experiment. The results unveil that the dramatic thermal conductivity reduction, about 83% from 300 to 800 K, originates from the enhanced four-phonon process. Our insights on the thermal transport mechanisms might benefit the materials design of thermoelectrics and thermal control.

DOI: 10.1103/PhysRevB.105.245204

I. INTRODUCTION

Thermoelectric materials can directly convert heat into electricity, which is crucial for waste heat harvesting and electricity production. The conversion efficiency is quantified by a dimensionless figure of merit, $zT = S^2\sigma\kappa^{-1}T$, where S is the Seebeck coefficient, T is temperature, σ is the electrical conductivity, and κ is the thermal conductivity [1]. High zT values are desirable for efficient heat conversion, but it is of grand challenge to achieve with both high electrical conductivity and low thermal conductivity since they are in general interrelated [1]. The Cu-based chalcopyrite compounds, such as $CuInTe_2$ and $CuGaTe_2$, have recently attracted extensive attention as heat harvesting materials [2–7]. They are characterized by the wide band gaps ($E_g \sim 1$ eV), absence of bipolar transport, and large Seebeck coefficient compared with the semimetals and narrow band-gap semiconductors. The space group of their crystal structure is $I\bar{4}2d$, with the high symmetric pseudo-cubic structure in long range and a distorted structure in short range [5,8]. Such a unique structure enables both moderate electrical conductivity and low heat conductivity, permitting high zTs. For example, $CuInTe_2$ possesses $zT \sim 1.18$ at 850 K [9], $zT \sim 1.4$ for $CuGaTe_2$ at 950 K [10], $zT \sim 0.91$ for $Cu_{2.1}Zn_{0.9}SnSe_4$ at 860 K [11], and $zT \sim 0.65$ for $Cu_{2.1}Cd_{0.9}SnSe_4$ at 700 K [12]. The high zTs of the Cu-based materials are mostly owing to the dramatic (up to 83%) reduction of the lattice thermal conductivity κ_l. For instance, the κ_l values of $CuInTe_2$ and $CuGaTe_2$ are about 6.0 and 7.4 $W\,m^{-1}\,K^{-1}$ at 300 K, in comparison with $\kappa \sim 1.0$ $W\,m^{-1}\,K^{-1}$ at 800 K. The reduction of κ_l in $CuInTe_2$ is over 83%, which is much higher than most common thermoelectrics [9,13–25]. Understanding the underlying physical mechanisms benefits material design of thermoelectrics. The abnormal κ_l reduction implies novel mechanism of thermal transport, which however, is still elusive.

There are three proposals for the mechanism of the unique thermal conductivity of chalcopyrite compounds [26–28]. The phonon avoided-crossing has been proposed to suppress the group velocity, resulted in large anharmonicity and low κ_l in the Ag-based chalcopyrite compounds [26]. The low-lying optical modes from theoretical calculation were supposed to couple with the acoustic phonon modes and generate the low avoided-crossing frequencies, illustrated by the Boson peaks of specific heat [26,29,30]. Examination of the phonon avoided-crossing is generally carried out by neutron scattering [31], but rare experimental efforts have been performed on the chalcopyrite compounds. It is still uncertain whether the phonon avoided-crossing is crucial for the Cu-based chalcopyrites. The lattice distortion is also proposed to cause the unique thermal conductivity. The phonon anharmonicity of the chalcopyrite compounds is suggested to be positively correlated to the lattice distortion based on the metavalent bonding nature of the cations [27]. The higher distortion of the selenides, like $AgInSe_2$ and $CuInSe_2$, results in the higher phonon anharmonicity and lower lattice thermal conductivity than tellurides, such as $AgInTe_2$ and $CuInTe_2$. To figure out the dramatic κ_l reduction of the Cu-based compounds, a

*pengqing@hit.edu.cn
†xjchen2@gmail.com

temperature treatment on the metavalent bonds should be further concerned. Recently, the soft optical modes have been reported by the negative Grüneisen parameters in $CuInTe_2$ [28]. The enhanced anharmonicity concerned with the softening of the optical modes has suppressed the κ_l from 11.7 to 4.1 $W\,m^{-1}\,K^{-1}$ upon compression [32]. This encourages a comprehensive study to reveal the phonon dynamics of $CuInTe_2$, especially the anharmonicity between the soft optical and acoustic modes. All the efforts point out, the importance of the phonon anharmonicity in the thermal transport properties of the chalcopyrite compounds. However, the proposals remain to be verified in the Cu-based chalcopyrites. Therefore, exploring the experimental methods to examine these proposals, especially to evaluate the phonon anharmonicity quantitatively, is desired to reveal the novel thermal transport behavior of the Cu-based compounds.

Raman spectroscopy is a well-established and routine method to study the phonon anharmonicity [33]. The phonon frequency and linewidth carry the essential information of the lattice anharmonicity. The reliability of this method has been proven in many materials, such as silicon [34,35], $Ge_{1-x}Si_x$ [36], ZnO [37], thermoelectrics [38,39], and 2D-materials [40,41]. Raman spectroscopy provides the same information of phonon anharmonicity as that from the neutron technique but with the advantages including high resolution and small samples [31,33,42,43]. It is a unique technique to detect the phonon modes with a wide temperature range and small temperature step, which makes the accurate quantitative analysis of the phonon evolution feasible [38,40,41].

$CuInTe_2$ has similar thermal transport behaviors as other Cu-based chalcopyrite compounds with the outstanding zT value [9]. Therefore $CuInTe_2$ is chosen as a model of the Cu-based chalcopyrite thermoelectrics. Both Raman scattering measurement and theoretical calculations are performed to investigate the thermal transport properties. The phonon dynamics is examined for three typical Raman modes. The frequency shift and linewidth variation obtained by Raman scattering measurement are used to evaluate the anharmonicity and validate the phonon scattering processes from computation. The phonon dispersion, group velocity, weighted phase space, scattering rate, mode-Grüneisen parameters, phonon lifetime, and thermal conductivity, are calculated to examine the results from Raman scattering measurement with both third-order and fourth-order anharmonicity. The mechanism of the drop of the κ_l above 300 K is discussed.

II. METHOD

A. Experimental details

The high-quality $CuInTe_2$ was prepared by melting the high purity elemental materials, namely, Cu, In, and Te (99.999% in purity). The detailed synthetic procedure can be referred to the literature [9]. To obtain strong signal of Raman spectra, the 532 nm laser is chosen. Laser transports through a circular pinhole and was vertically focused on the flat surface of specimen by a convex lens. The beam width was reduced to about 0.1 mm by the pinhole, then compressed to 5–8 μm by the convex lens. The laser power was kept at a low value of 1 mW to avoid damaging specimen. The power was carefully detected before collecting the spectra by a laser powermeter (Thorlabs PM100D). The measurements were divided into two stages of the low temperatures (7–300 K) and high temperatures (300–780 K). During the stage from 7 to 300 K, the Raman spectra were carried out in a helium continuous flowing cryostat. The sample had a regular geometric profile with a size of 100 μm $\times$ 80 μm $\times$ 54 μm. The temperatures were controlled by a temperature controller, using a heater and a Pt resistance temperature sensor close to the sample. During the stage from 300 to 780 K, a controlled atmosphere furnace was chosen to control the temperature. A quartz window with the high laser transparency was integrated in the furnace to avoid the signal interference. The sample used in high temperature was about 45 μm $\times$ 52 μm $\times$ 33 μm and sealed into the diamond chamber. To avoid the oxidation of the diamond, the chamber was continuously purged by the protecting gas, containing 97% argon and 3% hydrogen. The Raman spectra were collected every 10 K.

B. *Ab initio* calculations

The *ab initio* calculations were performed within the framework of Density Functional Theory (DFT) with the Perdew-Burke-Emzerhof (PBE) approximation [44] for exchange-correlation energy functionals. A plane-wave cutoff of 500 eV was used in all the calculations. The DFT calculations were carried out using the Vienna *ab initio* simulation package (VASP) [45] with the projector-augmented-wave (PAW) pseudopotentials [46]. The unit cell of $CuInTe_2$ contains 4 Cu atoms, 4 In atoms, and 8 Te atoms. The total energy and forces convergence criterion were 10^{-6} eV and 0.1 meV/Å, respectively, for geometry optimization and 10^{-8} eV and 10^{-6} eV/Å, for phonon calculations. The obtained lattice parameters were $a = b = 6.302$ Å and c=12.651 Å, in comparison with the experimental values of $a = b = 6.190$ Å and $c = 12.398$ Å [9]. The fully relaxed crystal structure was then used in the phonon calculations, which were carried out by the PHONOPY software package [47]. The second-order force constant and the phonon dispersion were obtained using a $2 \times 2 \times 1$ supercell with $6 \times 6 \times 6$ k grid.

The thermal conductivity was calculated by using the SHENGBTE software in the Boltzmann transport equation (BTE) framework [48]. The third-order and fourth-order anharmonicity were explicitly considered. The third-order force constant, controlling the three-phonon scattering rates, was obtained by combining the Thirdorder package and the density functional perturbation theory (DFPT) calculations in VASP [48]. The $2 \times 2 \times 1$ supercell with $8 \times 8 \times 8$ k-mesh was applied. The interaction range was set with a cutoff of 7.73 Å. The fourth-order force constant, controlling the four-phonon scattering rates, was calculated by combining the DFPT calculations of Fourthorder and the Fourphonon option of the SHENGBTE [49]. The 16-atom unit cell was employed for the calculation. The interaction range was 5.82 Å. The k mesh of $5 \times 5 \times 3$ was used in the calculations. Besides the thermal conductivity, the phonon dynamics, including the weighted phase space, scattering rates, and mode-Grüneisen parameters, was also obtained by employing SHENGBTE with the q grid of $8 \times 8 \times 8$ and the scalebroad of 0.1. The definitions of the weighted phase space and scattering rate can be found in

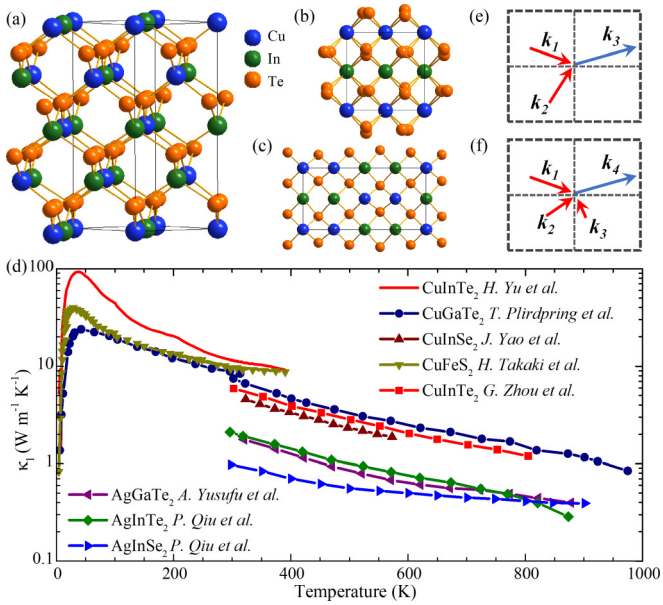

FIG. 1. The atomistic structure of $CuInTe_2$ in (a) tilt view; (b) top view; and (c) side view. (d) Comparison of the temperature dependent κ of I-III-IV_2 compounds including $CuGaTe_2$ [10], $CuGaSe_2$ [52], $CuFeS_2$ [53], $CuInTe_2$ [32,54], $AgGaTe_2$ [55], $AgInTe_2$ [56], and $AgInSe_2$ [56]. Diagrams of the (e) three- and (f) four-phonon scattering process.

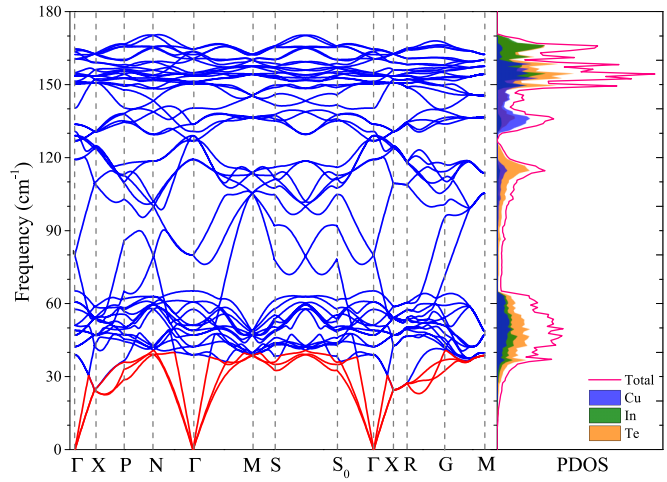

FIG. 2. Phonon dispersion and phonon density of states (PDOS) of $CuInTe_2$ from the theoretical calculations. (a) Phonon dispersion curves include the acoustic (optical) phonon modes represented by the red (blue) lines. (b) The total PDOS and the projected PDOS of Cu, In, and Te atoms are represented by red, blue, olive, and orange lines, respectively.

Refs. [49,50]. The convergence of the results was checked in respect to parameters used in the calculations, including the cutoff of the interaction range, k mesh, and q grid.

III. RESULTS AND DISCUSSION

A. Structure and thermal conductivity

$CuInTe_2$ has a tetragonal structure with the space group of $I\bar{4}2d$ (space group number 122) [51]. The view of atomistic configurations from tilt (1.3,1,−0.02), top (0,0,1), and side (1,0,0) is presented in Figs. 1(a), 1(b) and 1(c), respectively. Cu and In atoms sit on the vertices of the distorted tetrahedrons, connecting with the center Te atoms in different bond lengths and angles [5]. The asymmetric bonding configuration has been considered to benefit the phonon anharmonicity in $CuInTe_2$ [27].

The thermal conductivities of $CuInTe_2$ and several typical chalcopyrite compounds are compared in Fig. 1(d) [10,32,52–56]. The κ_l curves follow the common λ shape, suggesting a universal heat transport mechanism. The heat transport behavior at low temperatures is attributed to the phonon scattering at grain boundaries, and that at high temperatures is due to phonon anharmonicity [57]. The maximum value of κ_l is a result of the crystallite dimension [58]. With the increment of temperature beyond that corresponding to the peak value, the reduction of κ_l is a result of the phonon-phonon scattering. The multiple phonon processes originate from the anharmonicity, including three- and four-phonon scattering processes, as schematically shown in Figs. 1(e) and 1(f), respectively. Interestingly, the κ_l reduction of a Cu-based chalcopyrite is larger than that of an Ag-based compound. In the $CuInTe_2$ case, the κ_l is reduced by 83% from 300 to 800 K. This severe reduction of κ_l implies the unusual thermal transport properties of Cu-based compounds.

B. Phonon dispersion curves

We have calculated the phonon dispersion curves and the phonon density of states (PDOS) of $CuInTe_2$, as shown in Fig. 2. The frequencies of all the phonon modes are below 180 cm^{-1}. There are no imaginary frequencies in the phonon dispersion curves for all phonon modes, evidencing that the system is dynamically stable. Both the phonon dispersion curves and PDOS curves show that the phonon energy band gaps or forbidden energies are absent in the whole frequency range. The nonexistence of phonon bandgap permits abundant phonon-phonon scattering processes in $CuInTe_2$. Three main PDOS peaks are positioned around 60, 120, and 150 cm^{-1}. We can roughly divide the phonon modes into three domains: low-frequency (<70 cm^{-1}), medium-frequency (70–130 cm^{-1}), and high-frequency (>130 cm^{-1}) domains. The phonon frequencies at the Γ point are consistent with the previous theoretical calculations [27,54,59] and Raman scattering measurement [60,61].

Several low-energy optical modes can be observed around 60 cm^{-1}. These modes are separated by the acoustic modes at all the high symmetric k points except the G. This avoided-crossing behavior between the low-energy optical and acoustic modes is similar to that in the Ag-based chalcopyrites [26]. The lowest optical mode locates at the frequencies around 40 cm^{-1}, in comparison with the value about 30 cm^{-1} in $AgInTe_2$ and $AgGaTe_2$ [26]. A minimum frequency about 25 cm^{-1} can be observed at the X point, which is even lower than that of the $AgInTe_2$ and $AgGaTe_2$. For medium frequency phonons, the dispersion curves of the optical modes are characterized by large slopes, suggesting the large group velocity comparable with that of the acoustic modes. For high frequency phonons, the phonon curves are less dispersive, exhibiting lower group velocity

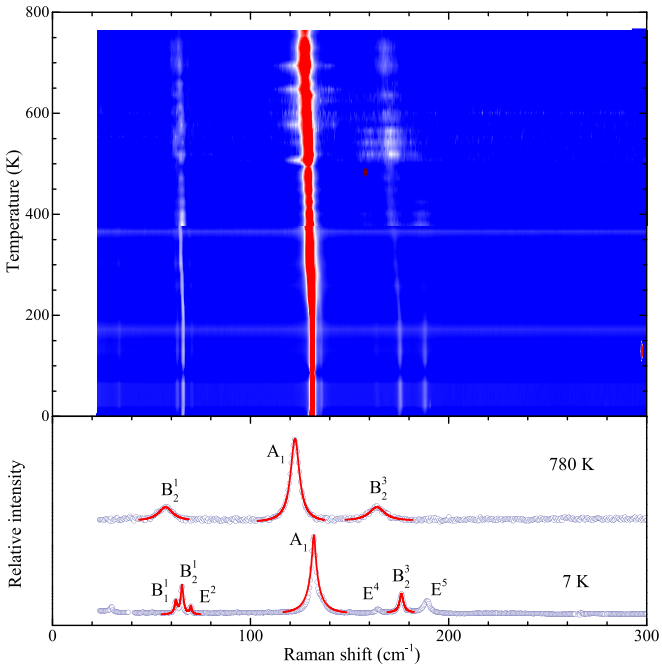

FIG. 3. Raman spectra of $CuInTe_2$ at the temperatures from 7 to 780 K. The lower part shows the Raman spectra at the lower (7 K) and higher (780 K) boundaries of temperatures. The blue cycles are the experimental value of the phonon modes. The solid red lines are the curves obtained by Lorentz fitting.

but higher PDOS. Besides the low-energy phonon modes, the other optical modes are nontrivial for the thermal transport at high temperatures. The investigation on the phonon dynamics should consider all phonon modes.

C. Raman measurement

The phonon anharmonicity of $CuInTe_2$ is reflected by Raman scattering. The spectra are collected from 7 to 780 K, which covers the temperature range for typical thermoelectric applications. The results are shown in Fig. 3. The $CuInTe_2$ primitive cell contains 8 atoms, thus 24 phonon modes. The symmetry assignments at Γ point are represented as $A_1 + 2A_2 + 3B_1 + 3B_2 + 6E$. Except A_2, the rest modes are Raman active [8,62]. In the lower panel, seven characteristic phonon modes are observed at 7 K. The central frequencies are about 62.3, 65.3, 70.2, 132.1, 164.2, 176.2, and 189.3 cm^{-1}. The values agree with both the calculation and Raman experiment [60,61]. The symmetry assignment of these modes can be determined as B_1^1, B_2^1, E^2, A_1, E^4, B_2^3, and E^5 respectively. When temperature increases, the phonon peaks of B_1^1, E^2, E^4, and E^5 vanish below 680 K. Only the B_2^1, A_1, and B_2^3 branches can be observed at 780 K. The spectra are drawn as a contour plot shown in the upper panel of Fig. 3. All the phonon branches display the softening of the frequencies and the widening of the linewidth with increasing temperature.

D. Phonon anharmonicity

1. Klemens-Hart-Aggarwal-Lax model

We have applied a semiquantitative theory to analyze the phonon anharmonicity. According to the Klemens-Hart-Aggarwal-Lax model [33], one phonon decays into two ($\omega_0 \rightarrow \sum \omega_n$, $n = 1, 2$) or three ($\omega_0 \rightarrow \sum \omega_m$, $m = 1, 2, 3$) phonons. The frequencies and linewidth can be expressed as functions of the cubic (three-phonon process) and quartic (four-phonon process) anharmonic terms:

$$\omega_i(T) = \omega_{i0} + A\left(1 + \sum_{n=1}^{2} \frac{1}{e^{\hbar\omega_n/k_BT} - 1}\right) + B\left[1 + \sum_{m=1}^{3}\left(\frac{1}{e^{\hbar\omega_m/k_BT} - 1} + \frac{1}{(e^{\hbar\omega_m/k_BT} - 1)^2}\right)\right], \quad (1)$$

$$\Gamma_i(T) = \Gamma_{i0} + C\left(1 + \sum_{n=1}^{2} \frac{1}{e^{\hbar\omega_n/k_BT} - 1}\right) + D\left[1 + \sum_{m=1}^{3}\left(\frac{1}{e^{\hbar\omega_m/k_BT} - 1} + \frac{1}{(e^{\hbar\omega_m/k_BT} - 1)^2}\right)\right], \quad (2)$$

where $\hbar$ is the reduced Plank constant, k_B is the Boltzmann constant, ω_{i0} and Γ_{i0} are the phonon frequency and linewidth at 0 K, ω_n and ω_m are the frequencies of the phonon participating the three-phonon and four-phonon processes, and A, B, C, and D are constants. The frequency shift $\Delta\omega_i(T_V)$ corresponding to the thermal expansion is obtained as follows:

$$\Delta\omega_i(T)_V = \omega_{i0}\left[\exp\left(-\gamma\int_0^T \alpha dT'\right) - 1\right], \quad (3)$$

where γ is the Grüneisen parameter and α is the thermal expansion coefficient. For the studied $CuInTe_2$, the γ values were 1.2 and 1.8, obtained from the experiments [28] and theoretical calculations [63] respectively. The α was 9.8×10^{-6} K^{-1}, obtained from the thermal expansion measurements [62].

The frequency shift of all the phonon modes caused by thermal expansion is less than 16 percents of the total shift in the temperature range from 7 to 780 K. The minor contribution from thermal expansion effect is thus ignored in the following analysis. The B_2^1, A_1, and B_2^3 branches are selected to investigate the phonon anharmonicity of $CuInTe_2$, because these phonons are representative modes in the three typical frequency domains (low, medium, and high frequency). They are corresponding to the peak values in PDOS and able to reveal the anharmonicity of $CuInTe_2$.

2. B_2^1 mode

The B_2^1 mode is a representative low-lying optical phonon branch in the low-frequency domain. The atomic vibration of this mode is shown in the inset of Fig. 4. The spectra of the B_2^1 mode are displayed in Fig. 4(a). The frequency is reduced from 65.3 (at 7 K) to 59.3 cm^{-1} (at 780 K), opposed to the behavior for the linewidth. The B_2^1 mode couples with the low-energy phonon modes, as the phonon avoided-crossing suggested [26,64]. The B_2^1 phonon probably decays into two phonons around 30 cm^{-1} (three-phonon process) or merge with two phonons around 60 cm^{-1} (four-phonon process). The scattering processes of the B_2^1 are considered in the softening of the frequency and the broadening of linewidth.

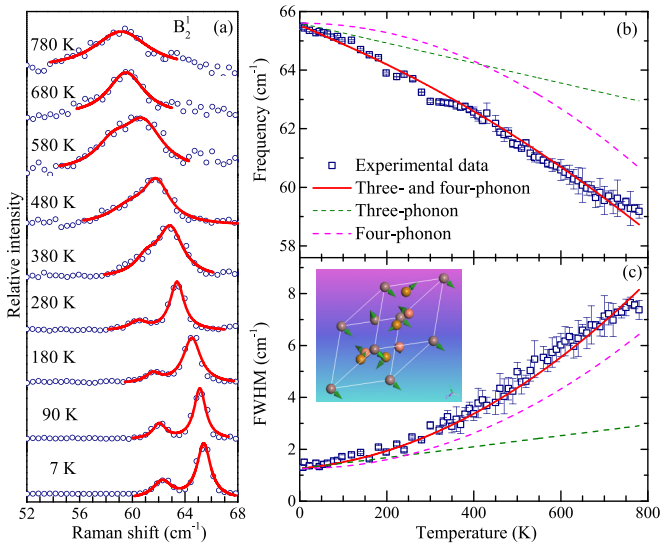

FIG. 4. (a) Raman spectra of the B_2^1 mode at temperatures from 7 to 780 K. The cycles are the raw data of the phonon modes. The curves are obtained by Lorentz fitting. (b) Frequency and linewidth of the B_2^1 mode are plotted as functions of temperature. The solid lines are the theoretical results. The dashed lines describe the cubic and quartic terms of the anharmonicity. The vibration directions of the atoms for the B_2^1 mode are indicated in the inset.

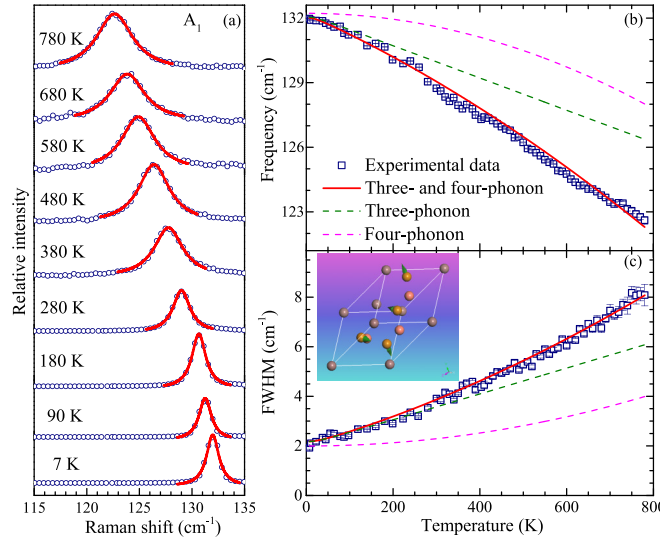

FIG. 5. (a) Raman spectra of the A_1 mode at the temperatures from 7 to 780 K. The cycles are the experimental data of the phonon modes. The curves are Lorentz fitting. (b) Frequency and linewidth of the A_1 mode are plotted as functions of temperature. The solid lines are the theoretical results. The dashed lines describes the cubic and quartic terms of the anharmonicity. The vibration directions of the atoms for the A_1 mode are illustrated in the inset.

The obtained results are plotted as functions of temperature in Figs. 4(b) and 4(c), in comparison with the experiment. The fitting curve matches the experimental values very well. The fitting parameters are summarized in Table I. Both three-phonon and four-phonon processes contribute to the phonon anharmonicity. For a clear view, the cubic and quartic terms are compared in Fig. 4. At the low temperatures below 300 K, the frequency and linewidth evolutions roughly follow the cubic term. Above 300 K, the curves significantly deviate from the cubic term. This deviation implies the fourth-phonon scattering of the B_2^1 mode is nontrivial.

3. A_1 mode

The A_1 mode represents the phonon branches in the medium-frequency range from 70 to 130 cm^{-1}. The Lorentzian function fitting of the A_1 mode is displayed in Fig. 5(a). The frequency and linewidth of this mode share similar behaviors to those of the B_2^1 mode as shown in Figs. 5(b) and 5(c). The frequency is reduced from 132.1 to 122.5 cm^{-1}, which is larger than that of the B_2^1 branch. The linewidth is enhanced from 2.1 to 8.0 cm^{-1}. Due to the high PDOS of the phonon modes around 60 cm^{-1}, the A_1 phonon most probably decays into two or three phonons with equal energies. The fitting results based on the Klemens-Hart-Aggarwal-Lax model are plotted together with the separated cubic and quartic parts. The frequency down-shifting and linewidth broadening are mainly caused by the third-order anharmonicity. The fourth-order anharmonicity becomes non-negligible above 500 K. Compared to the B_2^1 branch, one can see that the third-order anharmonicity is much higher, and the four-order anharmonicity is opposite. This may be attributed to the distinct atomic vibrations (seeing in the insert of Fig. 5).

4. B_2^3 mode

The B_2^3 mode, locating at 176.2 cm^{-1} at 7 K, is a typical phonon in the high frequency domain (above 130 cm^{-1}). The temperature dependent Raman spectra of the E^4, B_2^3, and E^5 branches are shown in Fig. 6(a). The E^4 and E^5 branches quickly vanish below 200 K, suggesting the low vibrational stability. As shown in Figs. 6(b) and 6(c), the frequency of the B_2^3 mode is reduced from 176.2 to 166.1 cm^{-1}. The linewidth increases from 1.6 to 12.1 cm^{-1}. B_2^3 mode with a large frequency locates at the top of the phonon dispersion plot. The possible scattering processes of this mode display as the phonon emission. The Klemens-Hart-Aggarwal-Lax model suggests the decisive three-phonon process below 350 K and the dominant four-phonon process at high temperatures. The B_2^3 mode exhibits a similar phonon anharmonicity to the B_2^1

TABLE I. Summary of the scattering parameters of ω_0 and Γ_0 for the B_2^1, A_1, and B_2^3 modes.

Mode	ω_0 (cm^{-1})	A (cm^{-1})	B ($\times 10^{-3}$ cm^{-1})	Γ_0 (cm^{-1})	C ($\times 10^{-1}$ cm^{-1})	D ($\times 10^{-3}$ cm^{-1})
B_2^1	65.48 ± 0.21	−0.04 ± 0.01	−6.92 ± 0.29	1.25 ± 0.20	0.26 ± 0.03	6.91 ± 0.27
A_1	132.22 ± 0.47	−0.21 ± 0.04	−1.52 ± 0.08	2.00 ± 0.19	1.82 ± 0.12	1.12 ± 0.09
B_2^3	177.03 ± 0.97	−0.23 ± 0.13	−4.12 ± 0.11	1.24 ± 0.12	1.15 ± 0.13	8.17 ± 0.23

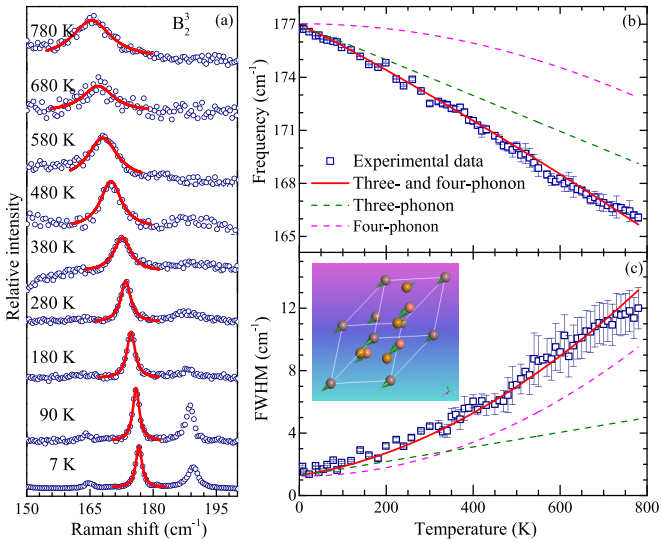

FIG. 6. (a) Raman spectra of the B_2^3 mode from 7 to 780 K. The blue cycles are the experimental data points. The solid red lines are Lorentz fitting. (b) The variation of Frequency and linewidth of the B_2^3 mode as functions of temperature. The solid lines are the theoretical results. The dashed lines describe the cubic and quartic terms of the anharmonicity. The vibrational directions of the atoms for the B_2^3 mode are indicated in the inset.

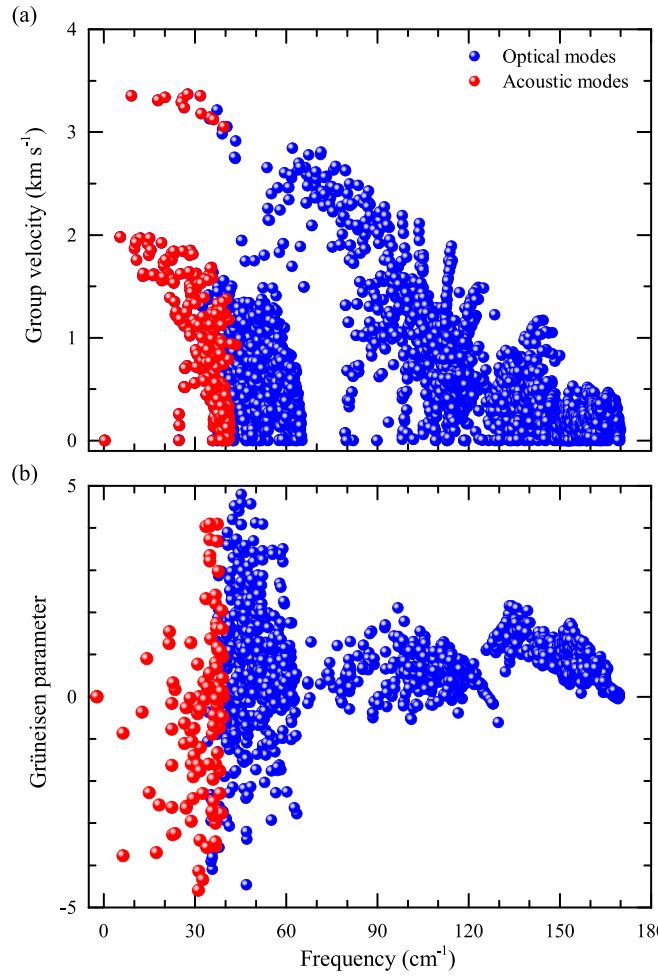

FIG. 7. The phonon group velocity (a) and mode-Grüneisen parameters (b) of $CuInTe_2$ from the theoretical calculations. The red dots represent the acoustic modes. The blue dots denote the optical modes.

mode, since the B_2^3 phonon is capable to have the reverse scattering processes of that of the B_2^1 phonon.

The experimental results reveal the phonon anharmonicity concerned with the scattering processes. The high third-order anharmonic parameter of A_1 mode demonstrates the strong third-order anharmonicity of the medium frequency phonon. On the other hand, the third-order anharmonicity of the B_2^1 and B_2^3 modes is extremely low when the temperature is below 300 K. The phonon scattering of the mode in the low-frequency domain is proposed to be frustrated by the low PDOS around 30 cm^{-1} or the weak coupling with the high-energy optical modes. The weak third-order anharmonicity and the absence of high-order scattering processes might be attributed to the relatively high κ_l about 6 $W\,m^{-1}\,K^{-1}$ at 300 K. When temperature is above 300 K, the four-phonon scattering of the B_2^1 and B_2^3 modes becomes dominant. The large fourth-anharmonicity of $CuInTe_2$ is beyond the proposals from previous investigations, pointing out a possible explanation on the dramatic κ_l reduction of the Cu-based chalcopyrites. To examine that, we calculate the κ_l by solving the Boltzmann transport equation with consideration of both third-order and fourth-order anharmonicity. The essential phonon dynamics, including the group velocity, mode-Grüneisen parameters, weighted phase space of the scattering processes, and the phonon lifetime, is also computed.

E. Phonon velocity and mode-Grüneisen parameters

The phonon velocity corresponding to the slope of the phonon dispersion is collected in Fig. 7(a). The phonon modes below 130 cm^{-1} are characterized by large group velocities. The group velocity of the acoustic modes is generally above 1 km/s. The value is suppressed around the frequency of 40 cm^{-1}, consistent with the avoided-crossing frequency. Besides, abnormally low group velocity below 1 km/s can be observed around 25 cm^{-1}. This is attributed to the lower avoided-crossing frequency at the X point.

The Grüneisen parameters are employed to weight the anharmonicity of the phonon modes, as shown in Fig. 7(b). Three peaks of the mode-Grüneisen parameters locate at the frequencies with high PDOS. The mode-Grüneisen parameters of acoustic and optical modes in the low-frequency domain (below 70 cm^{-1}) achieve the large absolute values above 2, suggesting the higher anharmonicity than the other phonon modes. The average mode-Grüneisen parameter is 1.38. The value is comparable with the experimental value of 1.2 [28] but lower than 1.96 and 1.8 from previous theoretical calculations [26,63]. Partial low-energy phonon modes possess the negative mode-Grüneisen parameters. Similar results have been reported in other chalcopyrite compound, such as $AgIn_{1-x}Ga_xTe_2$ [30]. These negative mode-Grüneisen parameters might be attributed to the metavalent bonding in chalcopyrites [27]. This result designates the instability of phonon vibration. It is usually associated with soft

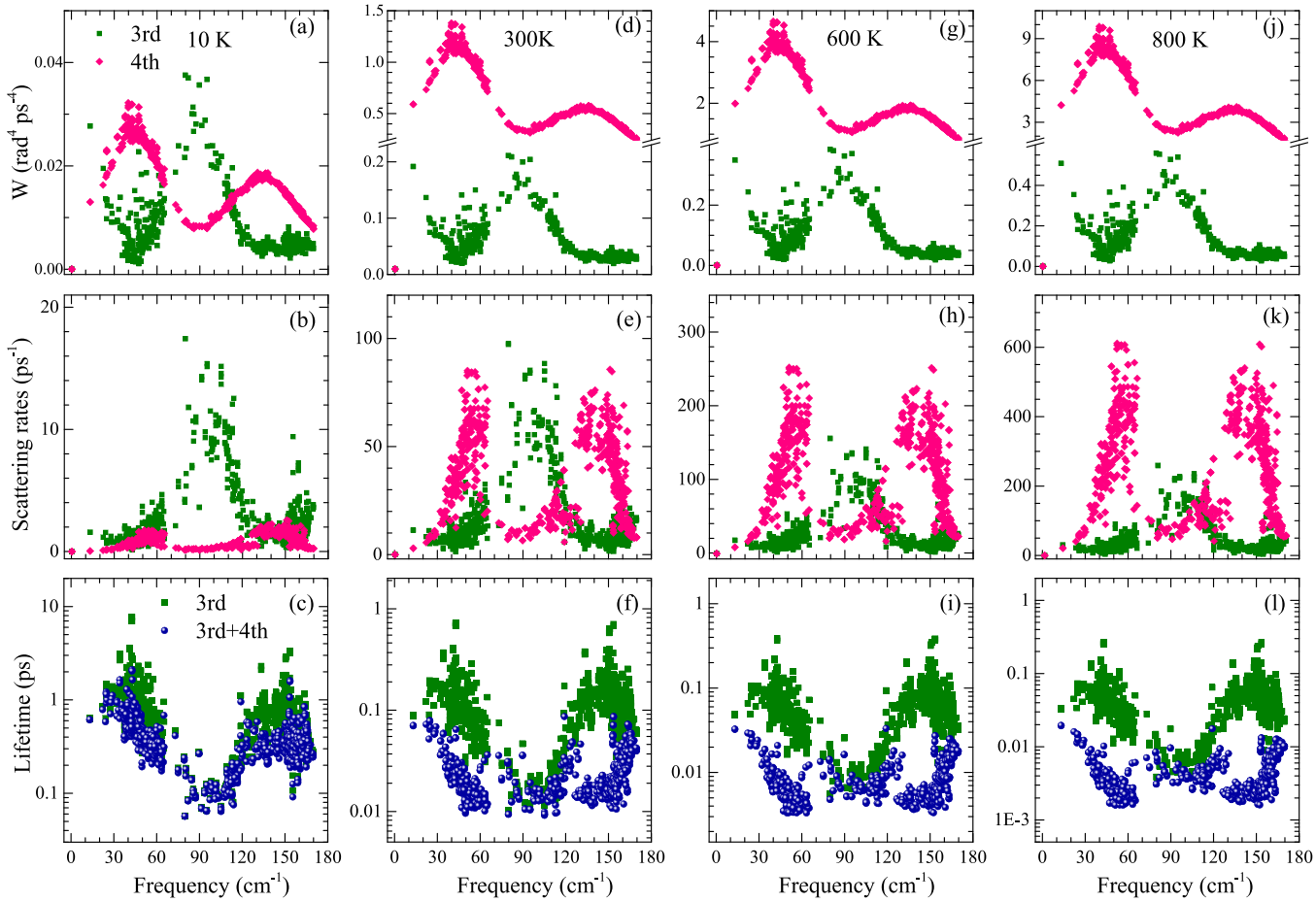

FIG. 8. The calculated phonon dynamics of the scattering processes with 3rd (third-order) and 4th (fourth-order) anharmonicity of $CuInTe_2$. [(a), (d), (g), and (j)] The weighted phase space of the phonon modes at 10, 300, 600, and 800 K, respectively. [(b), (e), (h), and (k)] The scattering rates calculated at 10, 300, 600, and 800 K, respectively. ([c), (f), (i), and (l)] The phonon lifetime calculated at 10, 300, 600, and 800 K, respectively. The weighted phase space, scattering rate, and phonon lifetime concerned with the three-phonon processes are denoted by the green squares. Those of the four-phonon processes are represented by pink rhombuses. The phonon lifetime with three-phonon and four-phonon processes are marked by navy dots.

anharmonic phonons under pressure. The B_1^1 and B_2^1 branches of $CuInTe_2$ have been demonstrated to be soft phonon modes by Raman scattering measurement under pressure [32], which denotes the large anharmonicity of the low-energy phonon modes.

F. Phonon dynamics, weighted phase space, scattering rate, and lifetime

The anharmonicity is directly related to the phonon scattering processes. To find out the origin, we have theoretically calculated the weighted phase space for the transition probabilities of the phonon scattering processes. The result at 10 K is given in Fig. 8(a). The three-phonon weighted phase space displays a broad peak around 100 cm^{-1}, illustrating the abundant three-phonon processes of the phonon modes within the medium frequency domain. When fourth-order anharmonicity is taken into account, two broad peaks centered around 40 and 150 cm^{-1} can be observed. The former peak is concerned with the absorption processes of the phonons in low-frequency domain. The later is related to the emission processes of the modes in high-frequency domain. This distinct difference manifests that the phonon modes in low- and high-frequency domains prefer four-phonon process rather than three-phonon processes. The scattering rates at 10 K are shown in Fig. 8(b). The three-phonon scattering rate displays a peak around 100 cm^{-1}. The four-phonon scattering rate is characterized by two small peaks around 50 and 150 cm^{-1}. The phonon modes within the medium frequency domain favor three-phonon processes due to the much larger scattering rates. However, the phonon modes in low- and high-frequency domains are rarely scattered, demonstrated by the low scattering rates of three-phonon and four-phonon processes.

When temperature increases, the weighted phase space of three-phonon and four-phonon processes are all enhanced [as in Figs. 8(e), 8(h) and 8(k)]. The four-phonon weighted phase space peaks at 800 K are more than 200 times higher than that at 10 K, in comparison with 20 times increment of the three-phonon ones. The maximum value of the four-phonon weighted phase space locates at 40 cm^{-1}, consistent with the avoided-crossing frequency of the low-energy phonon modes. This implies that the phonon coupling of the modes in low-frequency domain including acoustic and low-energy optical modes prefers the four-phonon processes.

Accompanied by the enhancement of the weighted phase space, the four-phonon scattering rates of the modes in low- and high-frequency domains are comparable to that of the three-phonon scattering rates of the modes within the medium frequency domain at 300 K, and the peaks are 2 and 3 times higher at 600 and 800 K respectively.

The phonon lifetime is determined by the scattering rate based on the relaxation time approximation [49]. The results are shown in Figs. 8(c), 8(f) 8(i), and 8(l). The phonon lifetime follows the V shape behavior at 10 K, which is governed by the three-phonon scattering processes. The large values of phonon modes in the low- and high-frequency domains are due to the low three-phonon scattering rates and the absence of high-order anharmonicity. Above 300 K, the phonon lifetime is suppressed, consistent with the enhancement of the scattering rates. The enhanced four-phonon scattering rates produce two deeps in the phonon lifetime around 50 and 150 cm^{-1}, but barely affect the modes in medium frequency domain.

The phonon dynamics from theoretical calculations totally supports the phonon anharmonicity from Raman scattering measurement. The dominant four-phonon weighted phase space of the phonon modes in low- and high-frequency domains evidences the large fourth-order anharmonicity of the B_2^1 and B_2^3 branches. Meanwhile, the low three-phonon weighted phase space value is consistent with low third-order anharmonic parameters. The A_1 branch corresponding to the phonons modes in the medium frequency is on the contrary. The abnormally large fourth-order anharmonicity of the B_2^1 and B_2^3 branches is further endorsed by the extraordinarily large four-phonon weighted phase space and scattering rate of the phonon modes in low-frequency and high-frequency domains at high temperatures. The fourth-order anharmonicity has been generally considered to be non-negligible at high temperatures. The pronounced four-phonon processes of $CuInTe_2$ at 300 K are intrinsically unusual for the traditional semiconductors, which could be accredited to the following three reasons. First of all, the phonon dispersion without any energy gap permits abundant phonon scattering processes in $CuInTe_2$. The high PDOS around 60 and 150 cm^{-1} benefits the four-phonon scattering of the modes around these frequency range. Secondly, the phonon coupling of phonon modes in low-frequency domain including the acoustic and low-energy optical modes encourages the four-phonon processes in $CuInTe_2$. Thirdly, the phonon modes available in these scattering processes have the relatively low frequencies less than 180 cm^{-1}, which are activated even at moderate temperatures. These factors promote the pronounced four-phonon processes in $CuInTe_2$. We thus think that the essential fourth-order anharmonicity is universal for the Cu-based chalcopyrite system, since they exhibit similar κ_l behavior over the temperature studied.

G. Lattice thermal conductivity

With the above parameters, we have obtained the κ_l behavior for $CuInTe_2$, as displayed in Fig. 9(a), together with the experimental data [54]. The κ_l only counting third-order anharmonicity overshoots the experimental value. It is less reduced at high temperatures. Similar results have been verified by previous works, suggesting the deficiency without

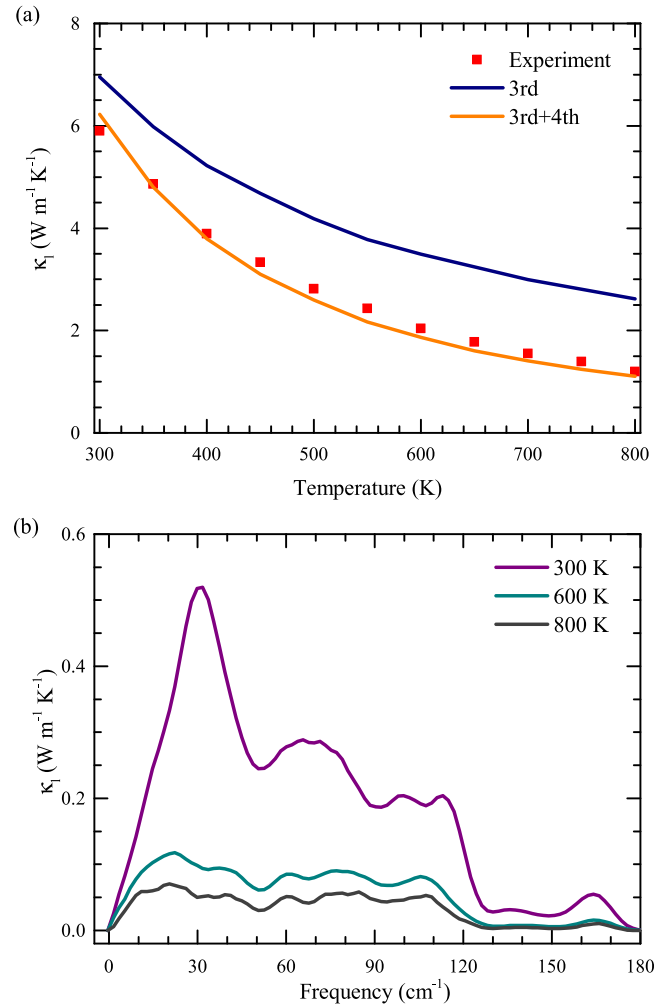

FIG. 9. Calculated lattice thermal conductivity of $CuInTe_2$ as functions of temperature (a) and frequency (b). (a) The navy line represents the thermal conductivity calculated with 3rd (third-order) anharmonicity. The orange line stands for the thermal conductivity calculated with both 3rd and 4th (fourth-order) anharmonicity. The red squares denote the experimental results from Ref. [54]. (b) Spectrally decomposed lattice thermal conductivity calculated at 300 (purple line), 600 (cyan line), and 800 K (gray line), respectively.

higher-order anharmonicity in $CuInTe_2$ [59,65]. By counting additional fourth-order anharmonicity, the κ_l is reduced by 10.5% over the value of only third-order anharmonicity at 300 K and 54.6% at 800 K. The recalculated κ_l curve is in good agreement with the experiments. Both the third-order and fourth-order anharmonicity contribute to the 83% κ_l reduction of $CuInTe_2$. In Fig. 9(b), the κ_l is plotted as a function of frequency to show the thermal conductivity contribution of each phonon mode. The phonons in low- and medium-frequency domains which are characterized by large group velocity and PDOS contribute most to the κ_l. With an increase in temperature, κ_l is reduced in the whole frequency ranges, particularly for the phonons in low-frequency domain.

Based on the dynamics of the phonon anharmonicity, the thermal transport behavior of $CuInTe_2$ can be revealed. The distinct temperature dependence behavior of the decomposed κ_l is related to the weighted phase space of the three-phonon

and four-phonon processes. The phonon modes in the low- and high-frequency domains mainly participate in the four-phonon process, and the anharmonicity of the phonon modes in the medium frequency domain acts as the three-phonon process. From 70 to 130 cm^{-1}, the κ_l is moderately reduced by the three-phonon scattering. The relatively high κ_l at low temperatures is a result of the weak third-order anharmonicity of the phonon modes below 70 cm^{-1}. Both third-order and fourth-order anharmonicity are responsible for the about 83% κ_l reduction of $CuInTe_2$. This pronounced reduction of the κ_l is due to the significantly enhanced fourth-order anharmonicity of the phonon modes below 70 cm^{-1}.

The dynamics of the phonon anharmonicity provides the crucial message about the thermal transport properties of $CuInTe_2$. The results are intrinsically distinct from the previous investigations [26,29,30]. The contribution of the acoustic phonon on the κ_l is overestimated by the phonon avoided-crossing. Based on our results, the phonon modes in medium frequency domain possess comparable group velocities with the acoustic modes. The three-phonon process of these modes, which is independent with the phonon avoided-crossing, is dominant for the κ_l behavior at low temperatures. Similar perspective has been examined on $CuGaS_2$, $CuGaTe_2$, $AgGaS_2$, and $AgGaSe_2$ by Raman or neutron scattering measurement [66–69]. However, the higher-order anharmonicity has been ignored due to the finite temperature range limited below 300 K. The phonon dynamics here in a wide temperature range from 7 to 800 K illustrates the abnormally large fourth-order anharmonicity in $CuInTe_2$. The fourth-order anharmonicity of the phonon modes in low-frequency domain has predominant contribution to the reduction of κ_l above 300 K.

It is worth noting the recent advances in modulating the κ_l of $CuInTe_2$ by applying external pressure [32]. The κ_l is significantly suppressed from 11.7 to 4.1 $W\,m^{-1}\,K^{-1}$, accompanied by the softening of the B_1^1 and B_2^1 branches. The lattice distortion has been confirmed to account for the phonon softening and the enhanced phonon anharmonicity [28], which is analogical to the doped $Cu_{1-x}In_xFeS_2$ [70], $Cu_{0.8+y}Ag_{0.2}In_{1-y}Te_2$ [71], and $Cu_{1-x-\delta}Ag_xInTe_2$ [72]. Our results might provide insights on these cases. The softening of the low-energy optical modes can be attributed to the negative Grüneisen parameters in low-frequency domain. The soft optical phonons suppress the group velocity of the acoustic modes. In addition, the peak of the four-phonon weighted phase space shifts to lower frequency. The fourth-order anharmonicity of the acoustic modes with lower energy is enhanced. Based on these factors, other chalcopyrite compounds are also expected to achieve low κ_l values via phonon softening through the lattice contraction. One possible way to have lattice contraction is to grow the chalcopyrite sample on the substrate with smaller lattice parameter.

IV. CONCLUSIONS

We have investigated the phonon dynamics of $CuInTe_2$ by Raman spectroscopy and theoretical calculations. The phonon anharmonicity has been examined over a wide range of temperature from 7 to 780 K. Based on the evolution of the frequency and linewidth, the phonon anharmonicity has been studied via the three representative modes of B_2^1, A_1, and B_2^3. The abnormally pronounced fourth-order anharmonicity of the B_2^1 and B_2^3 branches, corresponding to the phonon modes in low- and high-frequency domains, has been observed for the first time. The A_1 branch corresponding to the phonons in medium frequency domain from 70 to 130 cm^{-1} displays the three-phonon scattering. The essential phonon dynamics, including the group velocity, mode-Grüneisen parameters, weighted phase space of the scattering processes, phonon scattering rate, and the phonon lifetime, has been obtained by solving the Boltzmann transport equation. The results totally support the phonon anharmonicity from Raman scattering and provide detailed information to reveal the scattering processes of the phonon modes. The enhanced fourth-order anharmonicity of the low-energy modes has been found to be a direct result of the 200 times enhancement of the four-phonon weighted phase space. With the fourth-order anharmonicity, the temperature dependent κ_l curve from computation agrees with the experimental result, exhibiting the dramatic reduction over temperature. The fourth-order anharmonicity of the phonon modes in low-frequency domain has been confirmed to be crucial for the 83% reduction of the κ_l. This work thus contributes to understand the long-standing puzzle of the abnormal drop of the κ_l at high temperatures of the chalcopyrite compounds. Our results indicate that the κ_l of chalcopyrite compounds could be modulated via phonon engineering by introducing down-shift of the phonon modes through the techniques such as external lattice compression or stress.

ACKNOWLEDGMENTS

We thank Xun Shi, Li-Dong Chen, and Xiao-Ying Qin for fruitful discussions. This work at HIT was supported by the Shenzhen Science and Technology Program (Grant No. KQTD20200820113045081), the Basic Research Program of Shenzhen (Grant No. JCYJ20200109112810241), and the National Post-doctoral Program for Innovative Talents (Grant No. BX2021091). The work at HPSTAR was supported by the National Key R&D Program of China (Grant No. 2018YFA0305900).

[1] G. J. Snyder and E. S. Toberer, Complex thermoelectric materials, Nat. Mater. **7**, 105 (2008).

[2] P.-F. Qiu, X. Shi, and L.-D. Chen, Cu-based thermoelectric materials, Energy Storage Mater. **3**, 85 (2016).

[3] X. Shi, L.-D. Chen, and C. Uher, Recent advances in high-performance bulk thermoelectric materials, Int. Mater. Rev. **61**, 379 (2016).

[4] B. Wang, H.-J. Xiang, T. Nakayama, J. Zhou, and B.-W. Li, Theoretical investigation on thermoelectric properties of Cu-based chalcopyrite compounds, Phys. Rev. B **95**, 035201 (2017).

[5] J.-W. Zhang, R.-H. Liu, N. Cheng, Y.-B. Zhang, J.-H. Yang, C. Uher, X. Shi, L.-D. Chen, and W.-Q. Zhang, High-performance pseudocubic thermoelectric materials from

non-cubic chalcopyrite compounds, Adv. Mater. **26**, 3848 (2014).

[6] F.-J. Fan, L. Wu, and S.-H. Yu, Energetic I-III-VI_2 and I_2-II-IV-VI_4 nanocrystals: synthesis, photovoltaic and thermoelectric applications, Energy Environ. Sci. **7**, 190 (2014).

[7] M. G. Panthani, V. Akhavan, B. Goodfellow, J. P. Schmidtke, L. Dunn, A. Dodabalapur, P. F. Barbara, and B. A. Korgel, Synthesis of $CuInS_2$, $CuInSe_2$, and $Cu(In_xGa_{1-x})Se_2$ (CIGS) nanocrystal "inks" for printable photovoltaics, J. Am. Chem. Soc. **130**, 16770 (2008).

[8] C. Rincón and F. J. Ramírez, Lattice vibrations of $CuInSe_2$ and $CuGaSe_2$ by Raman microspectrometry, J. Appl. Phys. **72**, 4321 (1992).

[9] R.-H. Liu, L.-L. Xi, H.-Li. Liu, X. Shi, W.-Q. Zhang, and L.-D. Chen, Ternary compound $CuInTe_2$: A promising thermoelectric material with diamond-like structure, Chem. Commun. **48**, 3818 (2012).

[10] T. Plirdpring, K. Kurosaki, A. Kosuga, T. Day, S. Firdosy, V. Ravi, G. J. Snyder, A. Harnwunggmoung, T. Sugahara, Y. Ohishi, H. Muta, and S. Yamanaka, Chalcopyrite $CuGaTe_2$: A high-efficiency bulk thermoelectric material, Adv. Mater. **24**, 3622 (2012).

[11] M.-L. Liu, F.-Q. Huang, L.-D. Chen, and I.-W. Chen, A wide-band-gap *p*-type thermoelectric material based on quaternary chalcogenides of Cu_2ZnSnQ_4 (Q = S, Se), Appl. Phys. Lett. **94**, 202103 (2009).

[12] M.-L. Liu, I.-W. Chen, F.-Q. Huang, and L.-D. Chen, Improved thermoelectric properties of Cu-doped quaternary chalcogenides of $Cu_2CdSnSe_4$, Adv. Mater. **21**, 3808 (2009).

[13] B. Poudel, Q. Hao, Y. Ma, Y.-C. Lan, A. Minnich, B. Yu, X. Yan, D.-Z. Wang, A. Muto, D. Vashaee, and X.-Y. Chen, J.-M. Liu, M. S. Dresselhaus, G. Chen, and Z.-F. Ren, High-thermoelectric performance of nanostructured bismuth antimony telluride bulk alloys, Science **320**, 634 (2008).

[14] Y.-Z. Pei, X.-Y. Shi, A. Lalonde, H. Wang, L.-D. Chen, and G. J. Snyder, Convergence of electronic bands for high performance bulk thermoelectrics, Nature **473**, 66 (2011).

[15] C. B. Vining, W. Laskow, J. O. Hanson, R. R. Van der Beck, and P. D. Gorsuch, Thermoelectric properties of pressure-sintered $Si_{0.8}Ge_{0.2}$ thermoelectric alloys, J. Appl. Phys. **69**, 4333 (1991).

[16] B. C. Sales, D. Mandrus, and R. K. Williams, Filled skutterudite antimonides: A wew class of thermoelectric materials, Science **272**, 1325 (1996).

[17] H. Wang, J.-F. Li, M. Zou, and T. Sui, Synthesis and transport property of $AgSbTe_2$ as a promising thermoelectric compound, Appl. Phys. Lett. **93**, 202106 (2008).

[18] H.-Z. Zhao, J.-H. Sui, Z.-J. Tang, Y.-C. Lan, Q. Jie, D. Kraemer, K. McEnaney, A. Guloy, G. Chen, and Z.-F. Ren, High thermoelectric performance of MgAgSb-based materials, Nano Energy **7**, 97 (2014).

[19] S.-Y. Wang, J. Yang, L.-H. Wu, P. Wei, J.-H. Yang, W.-Q. Zhang, and Y. Grin, Anisotropic multicenter bonding and high thermoelectric performance in electron-poor CdSb, Chem. Mater. **27**, 1071 (2015).

[20] B. Zhong, Y. Zhang, W.-Q. Li, Z.-R. Chen, J.-Y. Cui, W. Li, Y.-D. Xie, Q. Hao, and Q.-Y. He, High superionic conduction arising from aligned large lamellae and large figure of merit in bulk $Cu_{1.94}Al_{0.02}Se$, Appl. Phys. Lett. **105**, 123902 (2014).

[21] A. Zevalkink, E. S. Toberer, W. G. Zeier, E. Flage-Larsen, and G. J. Snyder, Ca_3AlSb_3: An inexpensive, non-toxic thermoelectric material for waste heat recovery, Energy Environ. Sci. **4**, 510 (2011).

[22] W. Liu, X.-J. Tan, K. Yin, H.-J. Liu, X.-F. Tang, J. Shi, Q.-J. Zhang, and C. Uher, Convergence of Conduction Bands as a Means of Enhancing Thermoelectric Performance of *n*-Type $Mg_2Si_{1-x}Sn_x$ Solid Solutions, Phys. Rev. Lett. **108**, 166601 (2012).

[23] H.-J. Pang, C.-G. Fu, H. Yu, L.-C. Chen, T.-J. Zhu, and X.-J. Chen, Origin of efficient thermoelectric performance in half-Heusler $FeNb_{0.8}Ti_{0.2}Sb$, J. Appl. Phys. **123**, 235106 (2018).

[24] L.-C. Chen, B.-B. Jiang, H. Yu, H.-J. Pang, L. Su, X. Shi, L.-D. Chen, and X.-J. Chen, Thermoelectric properties of polycrystalline palladium sulfide, RSC Adv. **8**, 13154 (2018).

[25] L.-C. Chen, P.-Q. Chen, W.-J. Li, Q. Zhang, V. V. Struzhkin, A. F. Goncharov, Z.-F. Ren, and X.-J. Chen, Enhancement of thermoelectric performance across the topological phase transition in dense lead selenide, Nat. Mater. **18**, 1321 (2019).

[26] Y. Cao, X.-L. Su, F.-C. Meng, T. P. Bailey, J.-G. Zhao, H.-Y. Xie, J. He, C. Uher, and X.-F. Tang, Origin of the distinct thermoelectric transport properties of chalcopyrite $ABTe_2$ (A = Cu, Ag; B = Ga, In), Adv. Funct. Mater. **30**, 2005861 (2020).

[27] L. Elalfy, D. Music, and M. Hu, Metavalent bonding induced abnormal phonon transport in diamondlike structures: Beyond conventional theory, Phys. Rev. B **103**, 075203 (2021).

[28] H. Yu, G. Huang, Q. Peng, L.-C. Chen, H.-J. Pang, X.-Y. Qin, P.-F. Qiu, X. Shi, L.-D. Chen, and X.-J. Chen, A combined experiment and first-principles study on lattice dynamics of thermoelectric $CuInTe_2$, J. Alloys Compd. **822**, 153610 (2020).

[29] H.-Y. Xie, X.-L. Su, X.-M. Zhang, S.-Q. Hao, T. P. Bailey, C. C. Stoumpos, A. P. Douvalis, X.-B. Hu, C. Wolverton, V. P. Dravid, C. Uher, X.-F. Tang, and M. G. Kanatzidis, Origin of intrinsically low thermal conductivity in Talnakhite $Cu_{17.6}Fe_{17.6}S_{32}$ thermoelectric material: Correlations between lattice dynamics and thermal transport, J. Am. Chem. Soc. **141**, 10905 (2019).

[30] X.-L. Su, N. Zhao, S.-Q. Hao, C. C. Stoumpos, M.-Y. Liu, H.-J. Chen, H.-Y. Xie, Q.-J. Zhang, C. Wolverton, X.-F. Tang, and M. G. Kanatzidis, High thermoelectric performance in the wide band-gap $AgGa_{1-x}Te_2$ compounds: Directional negative thermal expansion and intrinsically low thermal conductivity, Adv. Funct. Mater. **29**, 1806534 (2019).

[31] M. Christensen, A. B. Abrahamsen, N. B. Christensen, F. Juranyi, N. H. Andersen, K. Lefmann, J. Andreasson, C. R. H. Bahl, and B. B. Iversen, Avoided crossing of rattler modes in thermoelectric materials, Nat. Mater. **7**, 811 (2008).

[32] H. Yu, L.-C. Chen, H.-J. Pang, X.-Y. Qin, P.-F. Qiu, X. Shi, L.-D. Chen, and X.-J. Chen, Large enhancement of thermoelectric performance in $CuInTe_2$ upon compression, Mater. Today Phys. **5**, 1 (2018).

[33] M. Balkanski, R. F. Wallis, and E. Haro, Anharmonic effects in light scattering due to optical phonons in silicon, Phys. Rev. B **28**, 1928 (1983).

[34] J. Menéndez and M. Cardona, Temperature dependence of the first-order Raman scattering by phonons in Si, Ge, and α − Sn: Anharmonic effects, Phys. Rev. B **29**, 2051 (1984).

[35] B. C. Johnson, B. Haberl, J. E. Bradby, J. C. McCallum, and J. S. Williams, Temperature dependence of Raman scattering from the high-pressure phases of Si induced by indentation, Phys. Rev. B **83**, 235205 (2011).

[36] H. H. Burke and I. P. Herman, Temperature dependence of Raman scattering in $Ge_{1-x}Si_x$ alloys, Phys. Rev. B **48**, 15016 (1993).

[37] R. Cuscó, E. Alarcón-Lladó, J. Ibáñez, L. Artús, J. Jiménez, B.-G. Wang, and M. J. Callahan, Temperature dependence of Raman scattering in ZnO, Phys. Rev. B **75**, 165202 (2007).

[38] L.-C. Chen, Z.-Y. Cao, H. Yu, B.-B. Jiang, L. Su, X. Shi, L.-D. Chen, and X.-J. Chen, Phonon anharmonicity in thermoelectric palladium sulfide by Raman spectroscopy, Appl. Phys. Lett. **113**, 022105 (2018).

[39] F. Liu, P. Parajuli, R. Rao, P.-C. Wei, A. Karunarathne, S. Bhattacharya, R. Podila, J. He, B. Maruyama, G. Priyadarshan, J. R. Gladden, Y. Y. Chen, and A. M. Rao, Phonon anharmonicity in single-crystalline SnSe, Phys. Rev. B **98**, 224309 (2018).

[40] Z.-Y. Cao and X.-J. Chen, Phonon scattering processes in molybdenum disulfide, Appl. Phys. Lett. **114**, 052102 (2019).

[41] Y.-K. Peng, Z.-Y. Cao, L.-C. Chen, N. Dai, Y. Sun, and X.-J. Chen, Phonon anharmonicity of tungsten disulfide, J. Phys. Chem. C **123**, 25509 (2019).

[42] C.-W. Li, J. Hong, A. F. May, D. Bansal, S. Chi, T. Hong, G. Ehlers, and O. Delaire1, Orbitally driven giant phonon anharmonicity in SnSe, Nat. Phys. **11**, 1063 (2015).

[43] H.-J. Pang, L.-C. Chen, Z.-Y. Cao, H. Yu, C.-G. Fu, T.-J. Zhu, A. F. Goncharov, and X.-J. Chen, Mode Grüneisen parameters of an efficient thermoelectric half-Heusler, J. Appl. Phys. **124**, 195107 (2018).

[44] J. P. Perdew, K. Burke, and M. Ernzerhof, Generalized Gradient Approximation Made Simple, Phys. Rev. Lett. **78**, 1396(E) (1997).

[45] G. Kresse and J. Furthmuller, Efficient iterative schemes for ab initio total-energy calculations using a plane-wave basis set, Phys. Rev. B **54**, 11169 (1996).

[46] P. E. Blöchl, Projector augmented-wave method, Phys. Rev. B **50**, 17953 (1994).

[47] A. Togo and I. Tanaka, First principles phonon calculations in materials science, Scr. Mater. **108**, 1 (2015).

[48] W. Li, J. Carrete, N. A. Katcho, and N. Mingo, ShengBTE: A solver of the Boltzmann transport equation for phonons, Comput. Phys. Commun. **185**, 1747 (2014).

[49] Z.-R. Han, X.-L. Yang, W. Li, T.-L. Feng, and X.-L. Ruan, FourPhonon: An extension module to ShengBTE for computing four-phonon scattering rates and thermal conductivity, Comput. Phys. Commun. **270**, 108179 (2022).

[50] W. Li and N. Mingo, Thermal conductivity of fully filled skutterudites: Role of the filler, Phys. Rev. B **89**, 184304 (2014).

[51] A. M. Mintairov, N. A. Sadchikov, T. Sauncy, M. Holtz, G. A. Seryogin, S. A. Nikishin, and H. Temkin, Vibrational Raman and infrared studies of ordering in epitaxial $ZnSnP_2$, Phys. Rev. B **59**, 15197 (1999).

[52] J. Yao, N. J. Takas, M. L. Schliefert, D. S. Paprocki, P. E. R. Blanchard, H. Gou, A. Mar, C. L. Exstrom, S. A. Darveau, P. F. P. Poudeu, and J. A. Aitken, Thermoelectric properties of *p*-type $CuInSe_2$ chalcopyrites enhanced by introduction of manganese, Phys. Rev. B **84**, 075203 (2011).

[53] H. Takaki, K. Kobayashi, M. Shimono, N. Kobayashi, K. Hirose, N. Tsujii, and T. Mori, Thermoelectric properties of a magnetic semiconductor $CuFeS_2$, Mater. Today Phys. **3**, 85 (2017).

[54] G. Zhou and D. Wang, High thermoelectric performance from optimization of hole-doped $CuInTe_2$, Phys. Chem. Chem. Phys. **18**, 5925 (2016).

[55] A. Yusufu, K. Kurosaki, A. Kosuga, T. Sugahara, Y. Ohishi, H. Muta, and S. Yamanaka, Thermoelectric properties of $Ag_{1-x}GaTe_2$ with chalcopyrite structure, Appl. Phys. Lett. **99**, 061902 (2011).

[56] P.-F. Qiu, Y.-T. Qin, Q.-H. Zhang, R.-X. Li, J. Yang, Q.-F. Song, Y.-S. Tang, S.-Q. Bai, X. Shi, and L.-D. Chen, Intrinsically high thermoelectric performance in $AgInSe_2$ *n*-type diamond-like compounds, Adv. Sci. **5**, 1700727 (2018).

[57] M. G. Holland, Analysis of lattice thermal conductivity, Phys. Rev. **132**, 2461 (1963).

[58] J. Callaway, Model for lattice thermal conductivity at low temperatures, Phys. Rev. **113**, 1046 (1959).

[59] J. J. Plata, V. Posligua, A. M. Márquez, J. F. Sanz, and R. Grau-Crespo, Charting the lattice thermal conductivities of I-III-VI_2 chalcopyrite semiconductors, Chem. Mater. **34**, 2833 (2022).

[60] C. Rincón, S. M. Wasim, G. Marín, J. R. Huntzinger, A. Zwick, and J. Galibert, Raman spectra of the chalcopyrite compound $CuInTe_2$, J. Appl. Phys. **85**, 3925 (1999).

[61] C. Rincón, S. M. Wasim, and G. Marín, E. Hernández, J. M. Delgado, and J. Galibert, Raman spectra of $CuInTe_2$, $CuIn_3Te_5$, and $CuIn_5Te_8$ ternary compounds, J. Appl. Phys. **88**, 3439 (2000).

[62] H. Neumann, S. Physik, and K. M. Universität, Lattice vibrations in $A^IB^{III}C_2^{VI}$ chalcopyrite compounds, Helv. Phys. Acta **58**, 337 (1985).

[63] S. Sharma, A. Verma, R. Bhandari, and V. K. Jindal, *Ab initio* studies of structural, elastic and thermal properties of copper indium dichalcogenides ($CuInX_2$: X = S, Se, Te), Comput. Mater. Sci. **86**, 108 (2014).

[64] M. Baggioli, B. Cui, and A. Zaccone, Theory of the phonon spectrum in host-guest crystalline solids with avoided crossing, Phys. Rev. B **100**, 220201(R) (2019).

[65] Y.-H. Li, J.-Y. Liu, X.-Y. Wang, and J.-W. Hong, Anomalous suppressed thermal conductivity in $CuInTe_2$ under pressure, Appl. Phys. Lett. **119**, 243901 (2021).

[66] P. Derollez, J. Gonzalezb, B. Hennionc, and R. Fouret, Anharmonic properties of the $AgGaSe_2$ compound, Phys. B: Condens. Matter **305**, 191 (2001).

[67] J. González, E. Moya, and J. C. Chervin, Anharmonic effects in light scattering due to optical phonons in $CuGaS_2$, Phys. Rev. B **54**, 4707 (1996).

[68] J. Gonzalez, L. Roa, R. Fouret, P. Derollez, J. Lefebvre, and Y. Guinet, Anharmonic properties of soft modes in $CuGaS_2$ and $AgGaS_2$ chalcopyrite semiconductors, Phys. Status Solidi B **225**, R12 (2001).

[69] C. Rincón, S. M. Wasim, G. Marín, E. Hernández, and J. Galibert, Raman spectra of the chalcopyrite compound $CuGaTe_2$, J. Phys. Chem. Solids **62**, 847 (2001).

[70] H. Xie, X. Su, S. Hao, C. Zhang, Z. Zhang, W. Liu, Y. Yan, C. Wolverton, X. Tang, and M. G. Kanatzidis, Large thermal conductivity drops in the diamondoid lattice of $CuFeS_2$ by discordant atom doping, J. Am. Chem. Soc. **141**, 18900 (2019).

[71] H.-Y. Xie, S.-Q. Hao, S.-T. Cai, T. P. Bailey, C. Uher, C. Wolverton, V. P. Dravid, and M. G. Kanatzidis, Ultralow thermal conductivity in diamondoid lattices: High thermoelectric performance in chalcopyrite $Cu_{0.8+y}Ag_{0.2}In_{1-y}Te_2$, Energy Environ. Sci. **13**, 3693 (2020).

[72] R.-H. Liu, Y.-T. Qin, N. Cheng, J.-W. Zhang, X. Shi, Y. Grin, and L.-D. Chen, Thermoelectric performance of $Cu_{1-x-\delta}Ag_xInTe_2$ diamond-like materials with a pseudocubic crystal structure, Inorg. Chem. Front. **3**, 1167 (2016).